Revealing how internal sensors in a smart battery impact the local graphite lithiation mechanism

Annabel Olgo, Sylvie Genies, Romain Franchi, Cédric Septet, Quentin Jacquet, Quentin Berrod, Rasmus Palm, Pascale Chenevier, Elise Villemin, Claire Villevieille, et al.

nature communications

Article

https://doi.org/10.1038/s41467-024-54656-6

Revealing how internal sensors in a smart battery impact the local graphite lithiation mechanism

Received: 16 May 2024

Accepted: 14 November 2024

Published online: 26 November 2024

Check for updates

Annabel Olgo[1], Sylvie Genies[2], Romain Franchi[2], Cédric Septet[2], Quentin Jacquet[1], Quentin Berrod[1], Rasmus Palm[3], Pascale Chenevier[1], Elise Villemin[2], Claire Villevieille[4], Nils Blanc[5], Samuel Tardif[6], Olivier Raccurt[2] ✉ & Sandrine Lyonnard[1] ✉

Smart batteries, i.e., equipped with internal and external sensors, are emerging as promising solutions to enhance battery state of health and optimize operating conditions. However, for accurate correlations between the evolution of the cell parameters (e.g., temperature, strain) and physicochemical degradation mechanisms, it is crucial to know the reliability of sensors. To address this question, we perform a synchrotron operando X-ray diffraction experiment to investigate the local and global impact of the presence of internal sensors on a commercial prismatic Li-ion battery cell at various (dis)charge rates. We find that, while the overall electrochemical performance is unaffected, the sensors have a substantial impact on the local graphite lithiation kinetics, especially at high (dis)charge rates. These results show the importance of controlling local deformations induced by internal sensors and tailoring the dimensions of these sensors to obtain reliable battery performance indicators and optimize smart batteries.

Lithium-ion batteries (LIBs) are one of the leading technologies in modern energy storage solutions because of their high energy density and long lifetime[1]. In recent years, their use has become more significant[2] to meet the increasing demand for reducing carbon emission[3] and developing cleaner energy sources[4]. To meet demands for high-performance LIBs, improving their safety, durability, and performance has become essential—a challenge that prompts extensive research on advanced battery management systems (BMS), including methods to monitor the state of health (SoH) of a battery[5].

The SoH describes the degree of ageing of a battery cell and is obtained by comparing its observed specific capacity to the initial (or nominal) capacity[6]. It depends on the cell components (i.e., electrolyte, electrode materials, separator)[7–9] and on the operating conditions (i.e., charge rate (C-rate–1 C corresponds to charging a battery in one hour), state of charge range, and temperature)[10–14]. As a battery undergoes cycling, its SoH declines due to various degradation mechanisms[15] such as electrolyte and solid-electrolyte interphase (SEI) decomposition[16], parasitic reactions[17], Li-plating[18,19], and gas evolution[20]. These mechanisms contribute to ageing and can lead to safety concerns. For instance, Li-plating occurs on the graphite electrode at high current rates and/or low temperatures[21,22], leading to increased internal temperature, gas evolution, and finally, thermal runaway[17,23].

Smart batteries equipped with sensing technology like external and internal sensors offer promising solutions to enhance the durability and electrochemical performance and gain insight into degradation mechanisms[24–26]. Currently, these sensors are tested and developed for real-time monitoring of crucial parameters such as

[1]Univ. Grenoble Alpes, CEA, CNRS, Grenoble INP, IRIG, SyMMES, Grenoble, France. [2]Univ. Grenoble Alpes, CEA, LITEN, DEHT, Grenoble, France. [3]Univ. Tartu, Institute of Chemistry, Tartu, Estonia. [4]Univ. Grenoble Alpes, Univ. Savoie Mont Blanc, CNRS, Grenoble INP, LEPMI, Grenoble, France. [5]Univ. Grenoble Alpes, CNRS, Grenoble INP, Institut Néel, Grenoble, France. [6]Univ. Grenoble Alpes, CEA, IRIG, MEM, Grenoble, France. ✉e-mail: olivier.raccurt@cea.fr; sandrine.lyonnard@cea.fr

temperature[27–33], strain[29,34], gas pressure[35,36], and chemical composition[32,37–40]. Correlating the evolution of these parameters with electrochemical performance and physicochemical degradation mechanisms is one of the current challenges in the battery industry and represents the key to enhancing the safety and lifetime of batteries. As highlighted in numerous review papers[26,41–44], sensors provide critical insight into the origins of degradation and performance issues. By improving the chemical and physical properties of the sensors, we can obtain more accurate data, enabling effective dynamic response (e.g., self-healing), and consequently, enhance the safety and lifetime of the smart batteries[41,42]. Furthermore, Q. Meng et al.[44] emphasized the importance of developing advanced cloud BMS technology coupled with artificial intelligence (AI) to improve the accuracy of status assessment and operational reliability.

Among different sensor technologies, optical fiber (e.g., Fiber Bragg Grating (FBG)) sensors are promising candidates due to their small size, lightweight, fast response, chemical resistance, and immunity to electromagnetic fields[27,30]. The integration of FBG sensors into a battery for the real-time monitoring of internal temperature was first demonstrated by G. Yang et al.[37] J. Huang et al. estimated the formation of SEI and its structural changes in Na-ion and Li-ion battery cells thanks to an internal FBG sensor measuring temperature and pressure[32]. A few years later, they monitored the internal thermal changes (temperature and heat) of a commercial 18650 Na-ion cell with FBG, demonstrating the impact of various C-rates and ageing on internal temperature changes and thermodynamical parameters[40]. In addition to Li- and Na-ion batteries, FBG sensors have also been used in Li-metal batteries to monitor SEI growth and dendrite formation[45]. In the past few years, optical fiber sensors based on thermoluminescence have emerged to monitor internal temperature, as demonstrated by H. Li et al.[46]. and E. Villemin et al.[28]. E. Villemin et al. showed that the integrated sensor did not impact the overall electrochemical performance of the cell, enabling the real-time monitoring of internal temperature even at high C-rates[28]. More recently, Y. Wang et al.[47] used thermoluminescent probe to monitor the internal temperature variation during cycling with an accuracy of 0.1 °C.

Nonetheless, internal sensors are local probes, and their influence on the surrounding electrode material's state and behavior must be quantified and understood. For instance, the accuracy of reference electrode measurements might be overestimated, and methods to establish error quantification are crucial[48,49]. Additionally, inserting a sensor can mechanically disturb the electrode and separator layers, leading to potential leaks[50]. Clearly, a comprehensive understanding of how integrated sensors influence local reactions is essential to improve the accuracy of the data obtained with sensors and establish criteria for optimized smart batteries and BMS.

In this work, we provide insights into whether sensors affect local structural changes in the graphite electrode during battery cycling. We equipped a 1.1 Ah commercial prismatic lithium-ion battery pouch cell with two internal sensors—a reference electrode to monitor electrode potentials and a thermoluminescence-based optical fiber sensor for measuring internal temperature. We then performed an operando synchrotron X-ray diffraction (XRD) experiment to study this cell while cycling at low and high C-rates to determine if the probes influence the electrochemical response locally. Structural changes of the graphite electrode within the thick commercial cell were compared to a single-layer cell used as a benchmark for analyzing graphite staging. To investigate the geometrical impact of the temperature-sensitive sensor on the local lithiation mechanism and kinetics, we probed the commercial cell at three locations and spatially resolved the reaction mechanism across the multi-layer geometry at C/5 and 2 C rates. We show that the optical fiber disturbs the reaction kinetics in its vicinity, while the thinner reference electrode has a milder effect. Our results demonstrate that inserting sensors induces SoH measurement bias that may depend on sensor size and geometry.

Results

To understand the impact of probed sensors on local electrode lithiation mechanisms, we studied two graphite | |NMC622 lithium-ion battery cells: i) a commercial multi-layered prismatic cell in jelly-roll configuration equipped with a reference electrode and an optical fiber, and ii) a parent, non-equipped-single-layer-cell that was built using electrodes from the same dismounted and unrolled commercial cell. Details about sensor types and dimensions, materials used as anodes and cathodes, cell designs, dimensions, characteristics, and cycling protocols are provided in Supplementary Tables 1–6, Supplementary Figs. 1–6. We used a specific procedure to safely insert the sensors (Supplementary Fig. 3). The full process was implemented in a dry room with several steps to ensure no damage to the cell. First, the Li-FUN commercial cell was received in a dry state, hence not containing electrolyte and not activated yet. The integration of the sensors (fiber and reference electrode) was realized before the addition of the electrolyte and the initial SEI formation. Once the sensors were inserted, the cell was rewound and transferred into a glovebox, where it was activated by adding liquid organic electrolyte. As a final step, the cell was thermosealed and ready to be formed and cycled. Its electrochemical behavior is similar to the non-instrumented commercial cell and the home-made single-layer cell (Supplementary Fig. 6), proving the reliability of the cell assembly protocols. Both the instrumented multi-layer and the single-layer cells underwent a designed electrochemical sequence during the synchrotron experiment to access structural changes in operando mode at various cycling rates.

Principle of the operando XRD experiments

The principles of operando XRD experiments on the single-layer and commercial multi-layered cells are shown in Figs. 1b and 2c, respectively. The experiments were carried out in transmission geometry, and depth-averaged (through-plane) diffraction rings were captured and recorded by a 2D detector (see "Methods" for experimental details). Each radially-averaged diffraction pattern contains Bragg reflections arising from the various crystalline components, e.g., cell casing, current collectors, anode, and cathode layers. Diffraction data was collected from selected locations in the cells to obtain spatially resolved information on the graphite peaks' evolution specifically. This approach allows us to perform data quality control analysis – evaluation of beam effects and differences in local (in-plane) lithiation states– and to probe chosen areas localized in the vicinity of the inserted sensors. Note that the obtained data is depth-averaged; thus, we do not have information on through-plane concentration gradients that are reported to develop in the thickness of graphite electrodes, especially at high rates[51–54].

The single-layer cell was used as a reference cell to validate the operando XRD data acquisition and analysis methods, including the evaluation of the impact of the X-ray exposure conditions on the reaction processes. The data acquisition procedure of the single-layer cell at different locations is shown in Supplementary Fig. 7. The depth-averaged single-layer cell diffraction patterns obtained during the 1st charge-discharge cycle showed the expected evolution of the graphite (002) reflection (Fig. 1d) corresponding to the lithiation stages of graphite (Supplementary Fig. 8). However, local beam damage on the single-layer cell graphite electrode was observed at high C-rates when irradiating continuously one single point (Supplementary Fig. 9b). In contrast, XRD measurements performed at C/5 across 9-points (Supplementary Fig. 8). Short occasional control measurements (Supplementary Fig. 9c) taken at higher C-rates do not show any evidence of beam damage and, therefore, are suitable to analyze the lithiation mechanism. Overall, experimental data is in good agreement with the literature[55–58], confirming that the set-up and measurement protocols accurately describe the behavior of the single-layer cell. Details regarding the (de)lithiation mechanism and evolution of the Li_xC_6 phases are given in Supplementary Discussion 3.1. In-plane variations

https://doi.org/10.1038/s41467-024-54656-6

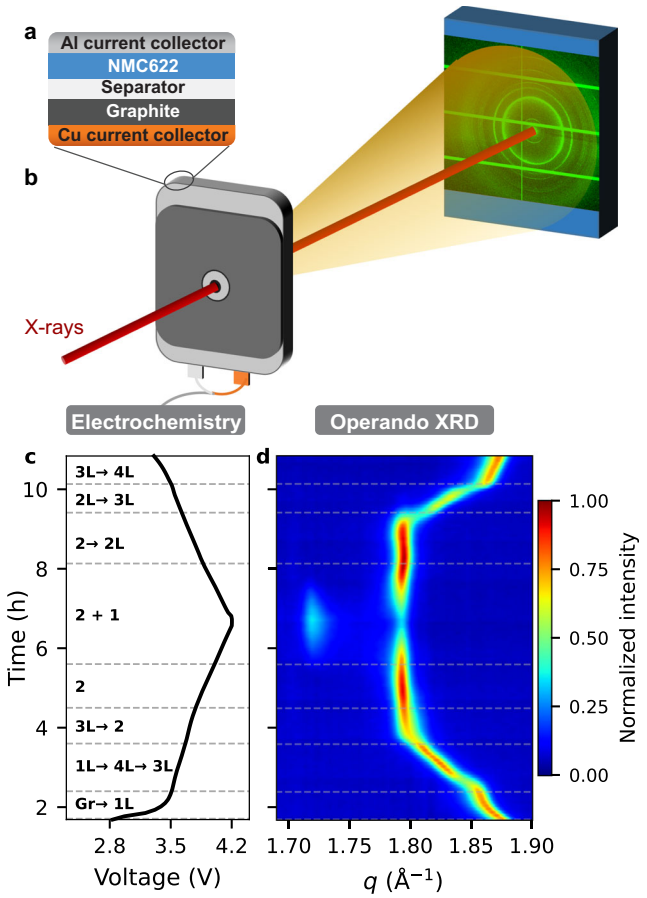

Fig. 1 | Operando XRD experiment set-up of the single-layer cell. a Top view of the single-layer cell mounted using a graphite negative electrode and an NMC622 positive electrode extracted from the prismatic commercial cell; **b** experimental set-up for operando XRD measurements using a 60*60 µm beam crossing in the middle of the single-layer cell through the hole, **c** The 1st cycle charge-discharge profile at C/5 showing the graphite staging process from graphite (Gr) to stage 1, where L stands for the liquid like ordering, and **d** corresponding stage transitions of graphite depicted as 2D-plot, showing the evolution of the (002) Bragg reflection in the q-range of 1.7–1.9 Å^{-1}, q being the momentum transfer. Source data are provided as a Source Data file.

of the lithiation state at the mm scale were evaluated by comparing operando XRD data acquired over 9 experimental points (3*3 grid measurements, Supplementary Fig. 10a). Variations in phase fractions in a fully lithiated state after charging at C/5 are less than 10% (Supplementary Fig. 8) over the probed area (Supplementary Fig. 7a), showing a quite homogeneous electrode behavior at this scale, as expected from industry grade commercial material.

Correlation between cell voltage, electrochemical potential, and temperature data of the multi-layered cell

The details on the instrumentation of the commercial cell and the cell handling, mounting, positioning on the X-ray beam, and sensors monitoring platform are provided in supporting information (Supplementary Figs. 11–15). Electrochemical parameters (i.e., cell voltage and electrode potential) and internal and external temperature of the cell were evaluated during the operando XRD acquisitions through the prismatic cell (Fig. 2, Supplementary Fig. 13, and Supplementary Table 7). The external temperature was monitored at various locations by thermocouples (labeled TC01 to TC07, Supplementary Fig. 12b), while the internal temperature was monitored by the optical fiber sensor (Fig. 2 and Supplementary Fig. 13) using the multicomponent detection & decoding system installed on the beamline (Supplementary Fig. 11).

The variations in cell voltage, NMC622 and graphite electrode potentials, luminescence signal, and external cell temperature are well correlated throughout the full cycling sequence, as shown in Fig. 2d–m. The electrochemical sequence (detailed in Supplementary Table 6) was designed to collect data during a standard low C-rate (C/5) cycle followed by conditions selected to induce significant heating within the battery: discharges at 4 C were applied during cycles three to six after fast charges at 2 C. First of all, we observe that the battery cell cycles well at high C-rates indicating that the sensors do not affect the global electrochemical response of the battery. The electrochemical performance is comparable to the non-instrumented multi-layered cell (Supplementary Table 5). However, there is a 5% reduction in capacity (from 1.39 Ah to 1.31 Ah at C/10), which may result from the amount of inactive area masked by both the reference electrode and fiber (Supplementary Discussion 3.1 and Supplementary Fig. 6a). Moreover, the cell behaves very similarly to the single-layer cell, as seen from the data plotted *vs* normalized capacity in Supplementary Figs. 6b–d. These results confirm the reliability of the assembling/forming processes.

From Fig. 2k–m, we can see that both the reference electrode and optical fiber operate and monitor the internal parameters of the cell. The LFP reference electrode exhibited stable behavior throughout the entire measurement. The NMC622 electrode potential evolution is in agreement with expected behavior ranging from 3–4.2 V *vs* Li$^+$/Li, and the local graphite electrode potential is far from the Li-plating potential in the charged state. Any measurement bias introduced by the reference electrode geometry would lead to an underestimated potential because of possibly increased ionic diffusion paths due to the insertion of the object in the cell structure. Therefore, the measured values for graphite, well above 0 V *vs* Li$^+$/Li, suggest that we are probing the lithium insertion conditions in the cell in the absence of plating, as desired. As expected, charging and discharging at a low C-rate of C/5 does not result in any detectable temperature change. In contrast, at high C-rates, an appreciable temperature elevation is produced both externally and internally (Fig. 2d–k, Supplementary Table 7, Supplementary Fig. 13). In particular, we note that the luminescence signal is clearly enhanced during the discharges at 4 C, as expected heat generation is proportional to the square of the current[59]. It reaches a value of 0.16 (arb. unit) in discharge at 4 C and 0.145 (arb. unit) in charge at 2 C (Fig. 2k, Supplementary Fig. 13h), corresponding to temperature rises of approximately 10 °C and 4 °C based on the luminescence-to-temperature response of the fiber[28].

Regarding the external temperature changes, the highest temperature increase was observed at the positive electrode tab (TC04), with a peak temperature of 36.08 °C, corresponding to a temperature increase of approximately 16.5 °C compared to the room temperature, during discharging at 4 C (Supplementary Table 7). In contrast, the smallest increase at 4 C was recorded at the negative electrode tab (TC02), reaching a maximum temperature of 30.9 °C. This difference can be attributed to the negative and positive electrode tab materials: the Al tab (positive electrode) has higher resistivity and poorer electric conductivity than the Cu tab (negative electrode), resulting in greater ohmic heating at the positive electrode[60]. Additionally, higher temperatures at 4 C were noted at the center of the cell (TC06 and TC07) compared to the areas near the reference electrode (TC01) and optical fiber (TC03). TC06 and TC07 exhibited a maximum temperature of 33.48 °C and 33.30 °C, respectively. In comparison, TC01 near the reference electrode demonstrated a maximum temperature of 31.65 °C and TC03 near the optical fiber 32.17 °C. The temperature rise distribution over the cell remains below <5 °C, and the internal temperature gradient, estimated from measurements by the fiber and TC06/TC07, is less than 1.5 °C. Overall, the observed external temperature changes at various C-rates (ΔT < 1 °C, < 5 °C, and < 15 °C, at C/5, 2 C, and 4 C, respectively) align well with results published on external temperature changes in LIBs[61,62].

https://doi.org/10.1038/s41467-024-54656-6

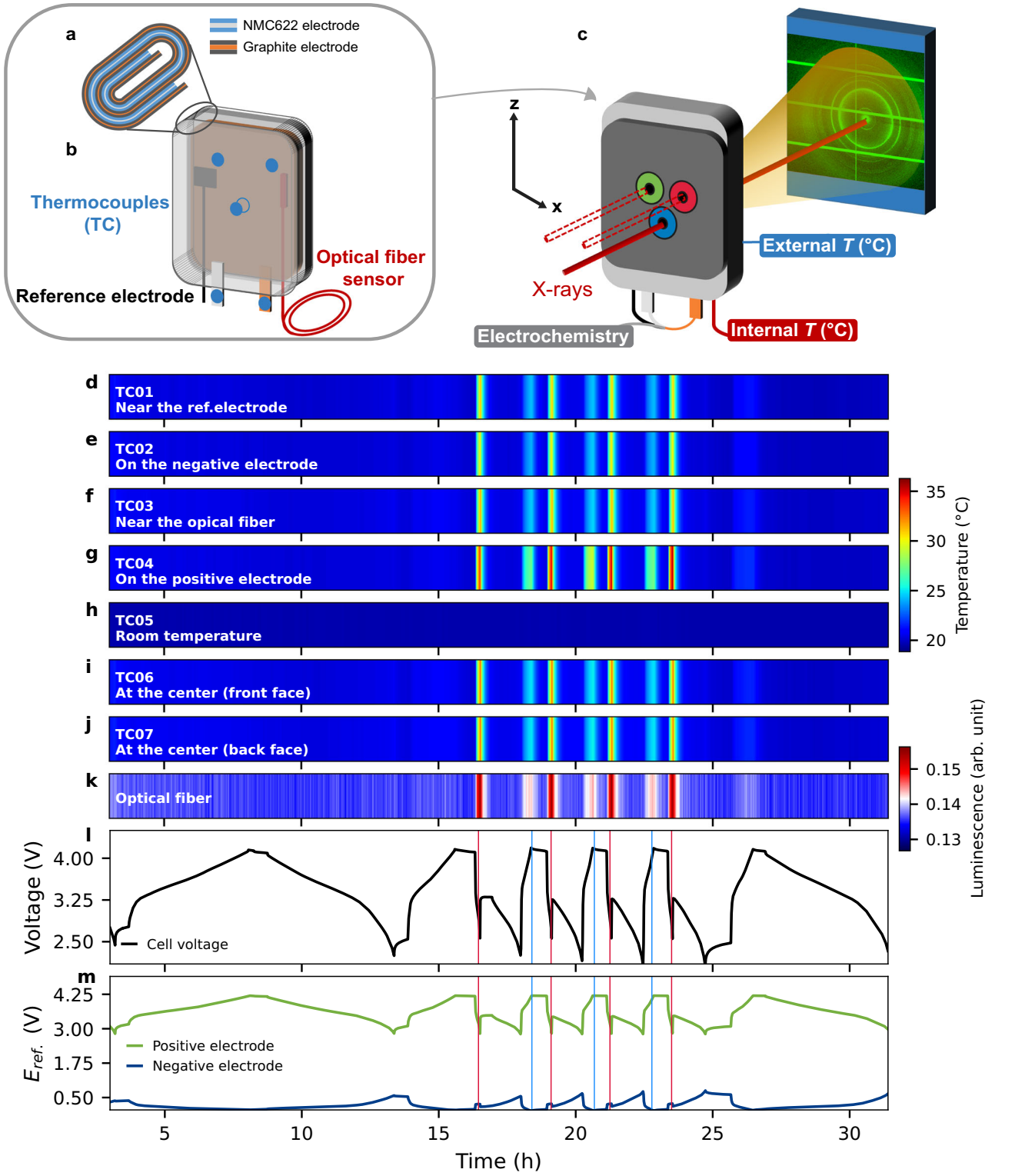

Fig. 2 | Operando XRD experiment set-up of the multi-layered cell and corresponding sensing data. a Top view of the commercial multi-layered prismatic pouch cell in a jelly-roll configuration with a double-coated graphite negative electrode and a double-coated NMC622 positive electrode and **b**–**c** experimental set-up to probe the multi-layered pouch cell equipped with external thermocouples, an optical fiber and reference electrode. The positions of external thermocouples (TC) are indicated with blue dots – filled blue dots indicate TCs positioned on the front face of the cell, and empty dots with blue contours indicate TCs located on the back face. The cell was scanned at three positions indicated by the colored holes to evaluate the central region (blue, far from sensors), the reference electrode region (green, on the reference electrode), and the region close to the optical fiber (red, at 500 microns from the fiber). The sensing data of (**d**–**j**) external thermocouples (Supplementary Fig. 12), and (**k**) the thermoluminescence optical fiber– the higher luminescence signal (arb. unit) indicates higher internal temperature. (**l**, **m**) Electrochemical sequence applied at various C-rates, from C/5 full cycle to fast charging (2 C) and discharging (4 C) conditions chosen to induce heat generation within the battery cell. Charge-discharge profiles of (**l**) the cell and (**m**) the NMC622 (green) and graphite (blue) electrodes obtained from the reference electrode from cycle 1 at C/5 to successive cycles with faster C-rates. The end of charging at 2 C and discharging at 4 C are highlighted with light blue and red lines, respectively. Source data are provided as a Source Data file.

This data indicates that i) both the cell and sensors respond consistently and with the expected behavior during the operando synchrotron XRD experiment, and ii) the increase in both internal and external temperature remains on average below 5 °C when fast charging the cell at 2 C. Based on these measurements, we selected the conditions best suited to evaluate the impact of sensor integration on the local graphite lithiation kinetics without significant perturbations from heating effects: we focused on the C/5 cycle data where there is no temperature change (< 1 °C) and on the charge at 2 C, where temperature changes are moderate (< 5 °C). An in-depth analysis of the fast discharge XRD data needed to uncover the possible interplay between local heating effects, sensors, and graphite kinetics is beyond the scope of this paper.

Graphite lithiation kinetics in the commercial multi-layered prismatic cell

To investigate the impact of the commercial multi-layered cell geometry on graphite lithiation kinetics, we compared the diffraction patterns collected at the center of the instrumented cell, away from the sensors, to those of the single-layer cell. The peak positions were determined as the center of mass (CoM) of the peak, which describes an averaged position obtained using weighted intensities distribution within the given q-range boundaries (q_{min}, q_{max}), as follows:

$$CoM = \frac{\int_{q_{\min}}^{q_{\max}} qI(q)dq}{\int_{q_{\min}}^{q_{\max}} I(q)dq} \quad (1)$$

Since the cells have different specific capacities, the state of charge (SoC) was used to compare graphite lithiation in both cells. SoC is defined as a ratio between the obtained (Q_{measured}) and nominal (Q_{nominal}) capacities, as follows:

$$SoC = \frac{Q_{measured}}{Q_{nominal}} * 100(\%) \quad (2)$$

The cells exhibited comparable behavior during charging at C/5, with minor differences due to the geometry of the multi-layer cell. Since the experiment was carried out in transmission mode, the diffraction pattern is the sum of individual diffraction patterns arising from the distinct layers of graphite stacked in the jelly-roll configuration. Due to the slight difference in the distance to the detector for each layer, the individual patterns are slightly shifted and sum up into a single Gaussian peak with a larger width than the reference resolution-limited graphite peak obtained in the single-layer cell. This is seen in the discharged state (Fig. 3a, top panel), where the multi-layered cell exhibits a slightly wider graphite peak, even though all graphite layers are expected to be identical. Moreover, the increased broadening observed at SoC 32% and 49% at C/5 (Fig. 3a) indicate a certain degree of through-plane heterogeneity developing across the various layers during the lithiation process. This might arise from i) varying lithium concentration gradients within each individual layer[51–54] and ii) layer-to-layer variations, which may result from a combination of factors, such as the local geometry of the cell, mechanical strains between layers, temperature gradients, preferential heat dissipation paths, etc. A higher resolution would be required to resolve the q-range shift of all the graphite electrode layers and, therefore, separately quantify the averaged lithium content in a given individual layer and potentially identify the origin of these layer-to-layer heterogeneities. As said earlier, access to the concentration gradients within one layer remains out of reach in a depth-averaged XRD experiment and requires through-plane scanning microdiffraction geometries[52,63]. Nevertheless, using the average cell data, we clearly see that, at the end of the charge, the two cells reach a very similar lithiated state characterized by the same LiC_{12}/LiC_6 ratio. Despite heterogeneities related to the distinct cell designs, both cells achieve comparable full lithiation states. Overall, the data demonstrate that we can effectively probe the thick prismatic cell with the operando XRD set-up in transmission and use the CoM as a relevant metric to quantify the averaged lithiation state at a low C-rate.

During the charge at 2 C, both the instrumented multi-layer and the single-layer cells exhibited broader diffraction peaks, indicating a more heterogeneous Li-ion distribution within the graphite electrode(s) (Fig. 3b). We found that, globally, through-plane electrode heterogeneities are slightly more pronounced for the multi-layered cell, as already observed at C/5.

Additionally, the multi-layered cell showed a distinct lag in its stage transitions at 2 C. At the onset of charging, it already exhibited a noticeably higher CoM value (CoM = 1.863 $Å^{-1}$) than the single-layer cell (CoM = 1.819 $Å^{-1}$) (Fig. 3b, top panel) due to the distinct states reached after completion of the first two cycles. The contrast between the cells became more prominent along charging, resulting in a modified CoM profile at low SoC (Fig. 3f), and the appearance of a shoulder peak (highlighted by ♦ in Fig. 3b).

Nonetheless, at higher SoC values (SoC > ~55%), the CoM of the multi-layered cell graphite peak became comparable again to the single-layer cell CoM. As no graphite peaks were detected at the end of the lithiation process, we know that all graphite regions were lithiated at the end, and the graphite electrode is fully active. Therefore, the shoulder peak indicates different kinetic pathways originating probably from ionic or electronic limitations in the multi-layer cell. These might result from stress distribution from internal and external embedded sensors and/or internal temperature gradients stemming from the jelly-roll configuration. Indeed, mechanical constraints might be induced by the external thermocouple located close to the X-ray beam path in the probed area (TC06 and TC07) or a reminiscent effect of deformation due to sensors, as will be discussed in the next section. Some drift in graphite lithiation due to severe localized heating cannot be excluded. Nevertheless, internal and external measures report a temperature rise distribution in the cell below <5 °C (Fig. 2g), and even smaller differences in temperature between internal (close to fiber) and external in the center of the cell temperatures (less than 1.5 °C).

The differences in the graphite electrode lithiation at a higher C-rate suggest a more heterogeneous lithiation process in the multi-layered cell, probably caused by differences in the SoC between graphite layers. At this stage, the peak-to-peak comparison with the single-layer cell usefully reveals the presence of through-plane heterogeneities induced by the prismatic design, which will be considered as a baseline for studying additional local lithiation differences induced by the optical fiber in its vicinity.

Impact of internal sensors on the commercial cell graphite electrode lithiation

We now analyze diffraction patterns obtained near the optical fiber (at a distance of ~500 microns) and in the region of the reference electrode to understand their impact on the local lithiation of the graphite electrode. The geometry of the X-ray acquisition conditions is schematized in Supplementary Fig. 14. Tomographic images of the fiber and reference electrode inserted in the cell are shown in Supplementary Fig. 15. The diffraction patterns acquired by scanning in the sensor areas are compared to the center of the cell data and shown in the supporting information (Supplementary Fig. 16) during charging at C/5 and 2 C.

At the beginning of charging at C/5, the profile of the graphite (002) peak is nearly identical between diffraction patterns collected in the reference electrode region, near the optical fiber, and at the center of the cell (Supplementary Fig. 16). Therefore, the initial discharged state is identical everywhere in the cell, and there is no intrinsic difference between the different locations in-plane. However, some differences were observed during the subsequent cycling.

Starting with the reference electrode region, we noticed the presence of a small additional peak at q = 1.805 $Å^{-1}$ in the delithiated state,

https://doi.org/10.1038/s41467-024-54656-6

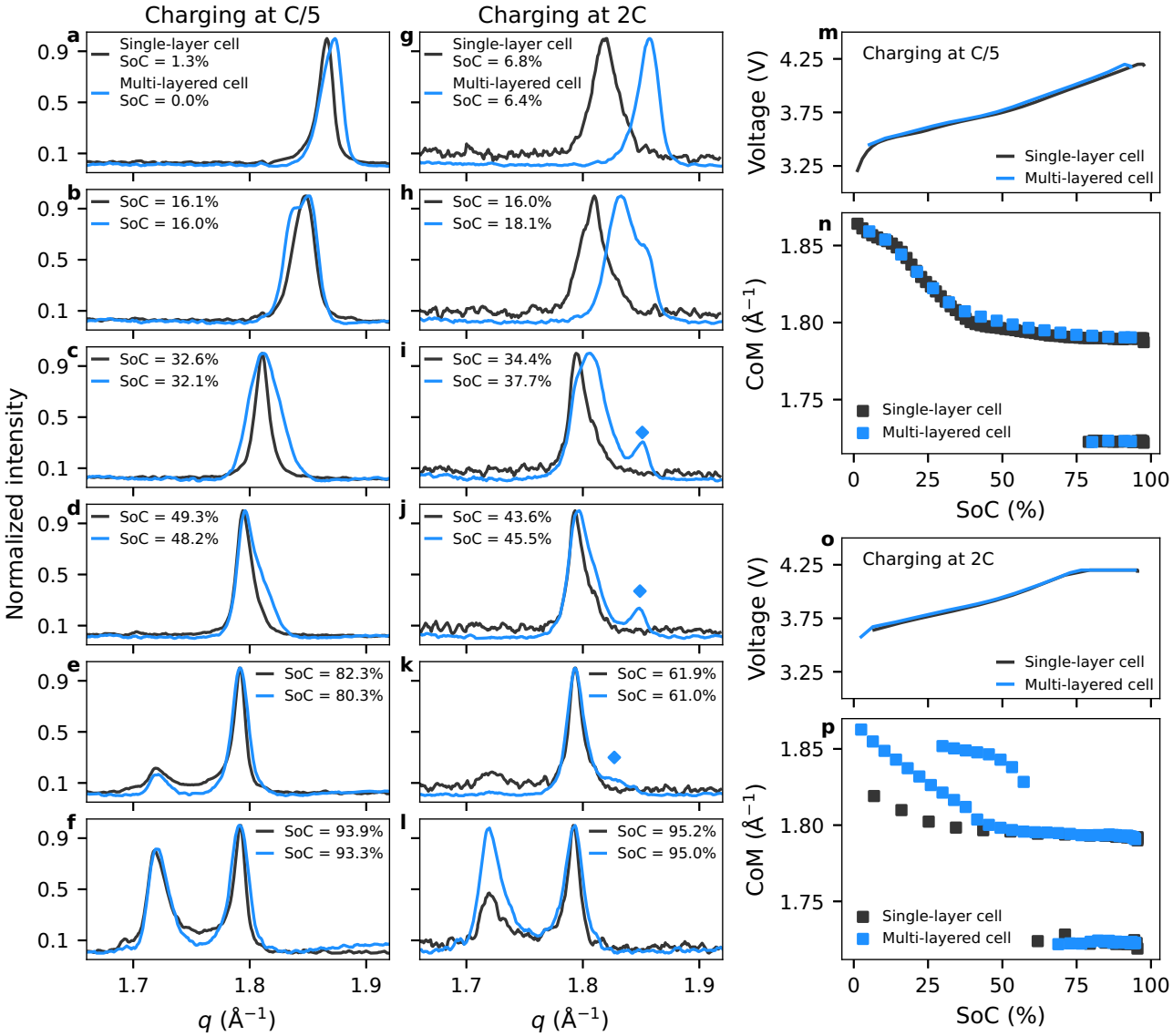

Fig. 3 | Effect of C-rate and cell design on graphite lithiation kinetics during charging. The multi-layered cell data are plotted in blue, and the single-layer cell data are plotted in black. Diffraction patterns show the evolution of the graphite (002), LiC_{12} and LiC_6 (001) peaks during charging (from ~0%, top, to ~95%, bottom) at (**a**–**f**) C/5 and (**g**–**l**) 2 C. Note that the initial peaks in C/5 data are very similar, indicating the same state of charge (SoC) in the initial fully delithiated state, while it is not the case in 2 C data due to a distinct delithiated state when the charge was started. Corresponding center of mass (CoM) (**n**, **p**) and cell voltage (**m, o**) *vs* SoC profiles at C/5 (**m**, **n**) and 2 C (**o**, **p**). Blue ◆ shows the presence and evolution of the shoulder peak in the multi-layered cell. Source data are provided as a Source Data file.

which is coming from the $LiFeO_4$ (LFP, the reference electrode material) (Supplementary Fig. 16a). Apart from this, the behavior is very similar to the one observed in the center of the cell, as seen from the similarity in peak positions and shape evolutions during the charging (Supplementary Fig. 16a–l), showing some peak broadening due to layered-dependent lags in lithiation, particularly at 2 C.

Concerning the optical fiber, we noticed small differences in peak shapes between the optical fiber location and the center of the cell during charging at C/5 (Supplementary Fig. 16a–f). These differences were attributed to a 4.5 min time interval between these two measurements (corresponding to a 1.5% difference in SoC). Additionally, we observed significant changes in the local graphite lithiation mechanism close to the optical fiber (Fig. 4). Indeed, at a voltage of 3.64 V during the 4 L → 3 L stage transition, a small additional peak at q = ~1.86 Å^{-1} was exclusively detected near the optical fiber (Fig. 4a–c, ◆). This well-separated peak was observed at all charging states (Fig. 4a). Interestingly, the SoC finally reached equilibrium during the hold step at 4.2 V, and no significant differences in SoC were observed near and far from the optical fiber (Fig. 4c). When charging at 2 C, the presence of such a delayed graphite phase around the optical fiber became more prominent (Fig. 4e–g). It remained present until the end of the hold step at 4.2 V (Fig.4g). Note that, as discussed before, a delayed graphite contribution was also observed at the center of the cell at such a high C-rate (Fig. 3b, f). However, the delay is clearly accentuated near the optical fiber. Moreover, the distinct separation between the delayed and normal graphite peaks near the optical fiber suggests considerable differences in SoC between the areas around the optical fiber and the center of the cell throughout charging. These results indicate the existence of "delayed graphite" areas located around the fiber, where the "delayed graphite" is an active but kinetically-limited graphite phase. The (de)lithiation process is severely delayed at high C-rates, revealing changes in local resistance and ionic pathways close to the fiber.

From this analysis, we conclude that the optical fiber has a considerable impact on the lithiation kinetics at the local scale, resulting in

https://doi.org/10.1038/s41467-024-54656-6

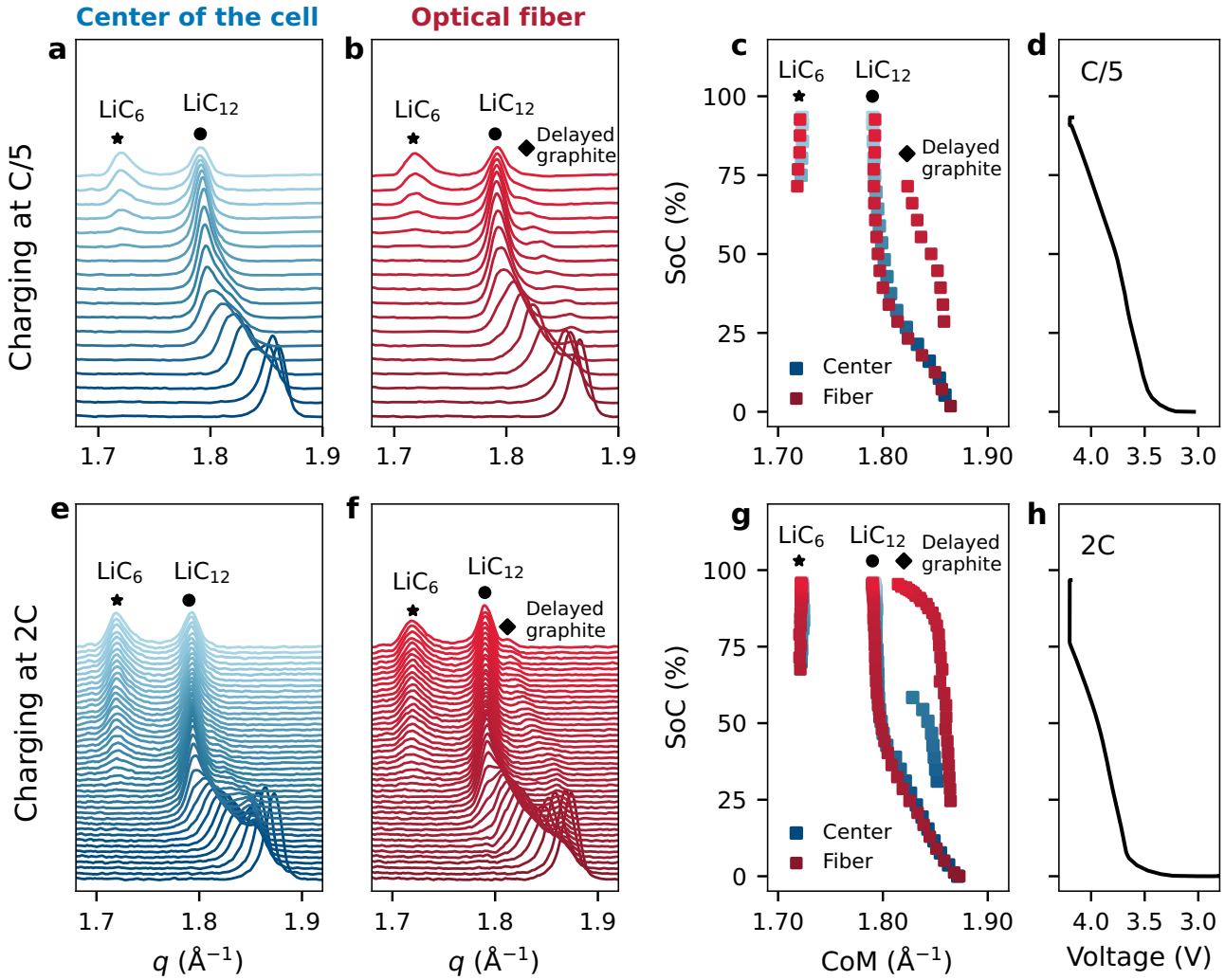

Fig. 4 | Effect of the optical fiber on local lithiation mechanism during charging. Diffraction patterns obtained at the center of the cell (**a**, **e**) and near the optical fiber (**b**, **f**) at C/5 (**a**, **b**) and 2 C (**e**, **f**). Evolution of state of charge (SoC) *vs* center of mass (CoM) (**c**, **g**) and *vs* cell voltage (**d**, **h**) at C/5 (**c**, **d**) and 2 C (**g**, **h**). Symbols *, ●, and ◆ correspond to LiC_6, LiC_{12}, and delayed graphite, respectively. Source data are provided as a Source Data file.

the formation of localized delayed graphite, which was observed throughout the charging at C/5 and 2 C at a distance of ~500 microns from the fiber. While charging at C/5, the delayed graphite finally caught up with the normal graphite at the end of the hold step, and no significant differences in the state of charge were observed between areas near the optical fiber, at the center of the multi-layered cell or in the reference electrode region. However, this delayed graphite became more prominent when the cell was charged at a higher C-rate of 2 C and stayed present even at the end of the hold step applied after charging. Therefore, although the presence of the optical fiber does not induce any detectable impact on the global electrochemistry measured at the cell level (Supplementary Fig. 6), it affects the lithiation in its vicinity, leading to localized differences in the lithiation state around the fiber. Note that the insertion of the reference electrode does not significantly disturb the local lithiation kinetics (Supplementary Fig. 16). On the opposite, the insertion of a bulky object such as the 200 μm-diameter optical fiber significantly deformed the electrode layers (Supplementary Fig. 15) and increased the distance between electrodes around it, which can explain the observation of locally hindered lithiation kinetics within the multi-layered cell throughout charging at various C-rates. In contrast, the presence of the smaller and flat reference electrode caused moderate deformations with limited spatial extensions and limited impact on the locally detected reaction kinetics. In the center of the cell, some reminiscent effects of the deformation induced by the sensors could be seen, showing that the perturbations due to device integration can extend inside the battery over large distances.

Discussion

This work focused on two fully operational battery cells: a commercial multi-layered pouch cell equipped with a reference electrode and temperature-sensitive optical fiber, and a single-layer cell, to understand the impact of the temperature-sensitive sensor on the lithiation kinetics and whether the data obtained near the optical fiber accurately represent the entire cell or exclusively the region around it. First of all, we found that, compared to the single-layered cell, the multi-layered cell showed a similar lithiation mechanism at a low cycling rate. Moreover, we showed that the commercial cell and the sensors were behaving as expected, showing the expected correlation between applied (dis)charging rates and changes in internal temperature. Clearly, there is no detectable impact of the inserted sensors on the averaged electrochemical performance of the commercial cell as quantified using standard macroscopic electrochemistry methods.

Nevertheless, the spatially-resolved synchrotron operando XRD experiment reveals microscopic-scale effects that are not detected using cell-averaged performance indicators. Our findings highlight

that graphite electrode lithiation kinetics are more delayed around the optical fiber than the rest of the cell. Thus, the information on the SoC obtained near the optical fiber exclusively describes this localized region, and uncertainties should be introduced while correlating locally measured strain with a global SoC or a lithiation degree of the graphite electrode. Such correlations may lead to over- or underestimating the graphite electrode lithiation degree and, therefore, decreased accuracy in SoH or SoC, especially at higher C-rates. Similarly, the detection of chemical species and reaction processes using various chemical-sensitive fibers or sensors should consider the lower reactivity in the deformed areas. One should be cautious when correlating locally measured parameters with chemical processes. For instance, during charging, intercalation of Li-ions into the graphite electrode results in volume expansions up to 13%[64], which is in clear correlation with strain evolution and thus can be used to estimate SoH and SoC[29,65]. This correlation can offer insight into capacity degradation, structural changes, and ageing mechanisms.

To summarize, we have shown that i) operational sensors can be embedded into large commercial battery cells without destroying the cell architecture or affecting the averaged performance, ii) an internal sensor can effectively provide a reliable measure of the averaged battery state if its size and aspect ratio do not disrupt the layered geometry locally, but iii) this internal sensor monitors a locally perturbed area and hence does not represent the cell behavior if it deforms the prismatic packing/stacking excessively. Further experiments and modeling are crucial for understanding the deformed electrode layers around an optical fiber and evaluating the current distribution around the sensor. An important aspect is quantifying the relation between the formation of locally different kinetics, the sensor characteristics, and the extent of induced deformations and mechanical changes in its vicinity. For instance, non-destructive high-resolution 3D imaging techniques such as synchrotron X-ray computed tomography could shed light on the topology of local deformations caused by the probed optical fiber sensor without disassembling the cell. It would be worth realizing 3D lithiation maps with high-resolution close-to, or even onto, specific sensors to further evaluate the extent of the perturbations and correlate them to design and fabrication processes. By understanding the deformations caused by an optical fiber, it could be possible to model differences in lithiation kinetics around the optical fiber and the rest of the cell and find criteria of sizes and shapes that minimize sensor perturbations. For instance, Guo et al.[66] studied the impact of the FBG sensor positioning in the z-direction and its size in a solid-state Li-metal cell, demonstrating the importance of both parameters on the cell's capacity and durability. In addition, Wang et al.[67] investigated the influence of sensor implantation and in-plane positioning on electrochemistry and internal temperature distribution. Tuning sensors' characteristics to reach the lowest impact on local cell behavior appears critical to optimize smart batteries. This will enable more accurate estimations of the SoC and SoH and help develop improved BMS.

Methods

Electrochemical cells

Two lithium-ion battery cells were studied in the operando synchrotron X-ray diffraction experiment—a commercial multi-layered prismatic cell equipped with sensors (Fig. 2a–c) and an unequipped single-layer cell (Fig. 1a, b) used as a reference to validate data acquisition and analysis protocols. Both cells consisted of $LiNi_{0.6}Mn_{0.2}Co_{0.2}O_2$ (NMC622) positive and graphite negative electrodes and were separated with a polyethylene (PE) separator with Al_2O_3 coating on the NMC622 side. The multi-layered cell, with a practical capacity of 1.1 Ah, was provided by Li-Fun Technology (Shuzhou, Hunan, China). The single-layer cell (25.6 mAh) was made by dismounting one 1.1 Ah cell to use the very same electrode materials and separator in the reference single-component measurements (Supplementary Fig. 2). The electrolyte used for both cells was 1 M $LiPF_6$ in mixture of ethylene carbonate (EC) and ethyl methyl carbonate (EMC) (3:7 in volume ratio) with 2 mass% of vinylene carbonate (VC) additive. The electrolyte volume added to the single-layer cell and multi-layered cell was 200 µl and 4 ml, respectively. Detailed information about both the single-layer and the multi-layered cell electrodes and their properties are provided in Supplementary Tables 2 and 3.

The multi-layered pouch cell with prismatic jelly roll configuration (Fig. 2a, Supplementary Fig. 3) was obtained from Li-Fun Technology in a dry state (without the electrolyte). The positive (NMC622) and the negative electrode (graphite) had a double-side coating, meaning both sides of a current collector were coated with the electrode material (Supplementary Fig. 4). The multi-layered cell was partially disassembled in a clean room where a reference electrode (LFP, $(Li_{(1-x)})FePO_4/LiFeO_4$, $E = 3.424$ V *vs* Li^+/Li)), and a temperature-sensitive sensor (thermoluminescent probe based on Gd_2O_2S particles doped with Er^{3+} and Yb^{3+}) were added into the cell (Fig. 2b, Supplementary Fig. 3). Both, the reference electrode and the temperature-sensitive sensor were placed between the NMC622 positive electrode and the separator. After embedding all the sensors, the jellyroll was rewound and then dried at 55 °C for 24 hours in a dynamic vacuum before being transferred to an argon-filled glovebox for the cell activation step. For the activation, 4 ml of $LiPF_6$ EC-EMC (3:7 vol%) + 2 wt% VC electrolyte was added to the cell.

Operando synchrotron X-ray diffraction (XRD) experiment

The operando synchrotron XRD experiment was conducted at European Synchrotron Radiation Facility (ESRF, Grenoble, France) on the beamline BM02[68]. The energy of the incident X-ray beam was fixed at 25 keV ($\lambda = 0.4959$ Å) and size at 60×60 µm. 2D-diffraction patterns were collected in transmission mode, allowing X-rays to pass through the samples, and recorded using an imXPAD WOS detector. The q-scale calibration was performed using chromium oxide (Cr_2O_3) and lanthanum hexaboride (LaB_6) as reference materials. The distance between the detector and the sample was 409 mm. In-depth averaged 1D XRD diffraction patterns were obtained by azimuthal integration of the recorded 2D patterns using the PyFAI library.

For the operando synchrotron XRD experiment, both cells were placed between metal plates (sample holder) to ensure mechanical stability and avoid displacements due to cell swelling (Fig. 1b, Fig. 2c, Supplementary Fig. 12a). To allow the X-ray beam to pass through the cell without interference from the sample holder, strategically positioned holes were drilled into metal plates. For the single-layer cell measurement, a single hole with a diameter of 1 mm was drilled through the metal plates at the center of the cell (Fig. 1b). 3×3 grid measurements were performed at low C-rates over 9 positions within a hole to evaluate local lithiation states and experimental errors (Supplementary Fig. 7a). Single-point measurements on control areas were also performed for beam evaluation (Supplementary Fig. 7b). For the multi-layered cell, three holes with a diameter of 1 mm were drilled in the reference electrode region, near the optical fiber, and at the center of the cell (Fig. 2c), respectively. Diffraction patterns were collected, ca. 500 microns from the optical fiber and on the reference electrode (Supplementary Figs. 14a and 15). The hole at the center of the cell was used to collect diffraction patterns from the mechanically undisrupted area.

Electrochemical cycling

The galvanostatic charge-discharge cycling of the cells under different current densities was conducted in two stages using a Biologic VMP3 cycler: i) initial formation cycles performed in our laboratory at 25 °C, and ii) electrochemical cycling during the operando synchrotron XRD experiment. The lower and upper cutoff voltages were set at 2.8 V and 4.2 V, respectively. All cycles consisted of charge and discharge at a constant current (CC). During the operando synchrotron XRD

experiment, each charge was followed by a constant voltage (CV) step at 4.2 V for one or two hours (the duration depended on the applied charging C-rate), followed by a short rest step (30 minutes) to stabilize the system and ensure the maximum state of charge. After every discharge, a rest step of 30 minutes to one hour was added to stabilize the cell's voltage. Detailed electrochemical protocols used during the formation process and operando synchrotron XRD experiment are provided in Supplementary Table 4 and Supplementary Table 6. The experimental set-up for monitoring the behavior of the reference electrode and optical fiber is shown in Supplementary Fig. 11.

Data analysis

The data acquired from the measurements was analyzed using the programming language Python on the Anaconda platform. Before the analysis, the collected data was processed in a series of steps using PRISMA Python package[69] Baseline removal was performed using the asymmetrical least squares function. After baseline removal, the q-range of each diffraction pattern was calibrated by aligning the experimental position of the Cu(200) peak with its corresponding theoretical value of 3.4756 $Å^{-1}$. Finally, peaks originating from the cell's casing, present in the diffraction patterns, were removed. In this work, only diffraction patterns from the single-layer cell measurement were suitable for fitting. Indeed, the multi-layer cell peaks have complex shapes due to the superposition of patterns originating from the different layers. The Pseudo-Voigt function (0.5 Lorentz function and 0.5 Gaussian functions) was used to fit the data obtained from the operando XRD experiment. Five distinct peaks corresponding to Li_xC_6 phases were observed in the first-order graphite region q-range (1.70–1.90 $Å^{-1}$). Hence, during the graphite (de)lithiation stages 1 L, 4 L, 3 L, 2 + 2 L, and 1, with peak bounds of 1.875–1.845 $Å^{-1}$, 1.840–1.825 $Å^{-1}$, 1.820–1.810 $Å^{-1}$, 1.799–1.777 $Å^{-1}$, and 1.725–1.705 $Å^{-1}$, respectively, were considered. Since the multi-layered cell diffraction patterns were not suitable for fitting peak positions in X-ray diffraction data, we chose to characterize graphite staging by the center of mass of the peak. It describes the intensity-weighted average peak position within the given q-range boundaries. Scipy.signal.find_peaks() function was used to determine the peaks in a diffraction pattern above a certain threshold level. All figures containing experimental results were made using Matplotlib Python library.

Data availability

The analyzed X-ray data generated in this study are provided in the Source Data file, as well as sensing and electrochemical data. The raw X-ray data that support the findings of this study are available in ESRF with the identifier https://doi.org/10.15151/ESRF-ES-675577547[68]. Data is under embargo until 2025 but could be released to the main corresponding author earlier on request. Analyzed data for all figures are provided in the Source Data Files, except for Figure S9 (a large set of diffraction data), which can be obtained at the request of the main corresponding author. Source data are provided with this paper.

References

1. Li, M., Lu, J., Chen, Z. & Amine, K. 30 years of lithium-ion batteries. *Adv. Mater.* **30**, 1800561 (2018).
2. Brudermüller, M., Sobotka, B. & Waughray, D. *A Vision for a Sustainable Battery Value Chain in 2030 Unlocking the Full Potential to Power Sustainable Development and Climate Change Mitigation*. 52 https://www3.weforum.org/docs/WEF_A_Vision_for_a_Sustainable_Battery_Value_Chain_in_2030_Report.pdf (2019).
3. *Communication from The Commission to The European Parliament, The European Council, The Council, The European Economic and Social Committee and The Committee of The Regions*. https://eur-lex.europa.eu/resource.html?uri=cellar:b828d165-1c22-11ea-8c1f-01aa75ed71a1.0002.02/DOC_1&format=PDF (2019).
4. Ritchie, H., Roser, M. & Rosado, P. *Renewable Energy*. *ourworldindata* https://ourworldindata.org/renewable-energy (2023).
5. Amici, J. et al. A roadmap for transforming research to invent the batteries of the future designed within the European large scale research initiative BATTERY 2030. *Adv. Energy Mater.* **12**, 2102785 (2022).
6. Fotouhi, A., Propp, K., Auger, D. J. & Longo, S. *State of Charge and State of Health Estimation Over the Battery Lifespan*. in *Behaviour of Lithium-Ion Batteries in Electric Vehicles: Battery Health, Performance, Safety, and Cost* (eds. Pistoia, G. & Liaw, B.) 267–288 (Springer International Publishing, Cham, 2018). https://doi.org/10.1007/978-3-319-69950-9_11.
7. Rana, S., Kumar, R. & Bharj, R. S. Current trends, challenges, and prospects in material advances for improving the overall safety of lithium-ion battery pack. *Chem. Eng. J.* **463**, 142336 (2023).
8. Liu, K., Liu, Y., Lin, D., Pei, A. & Cui, Y. Materials for lithium-ion battery safety. *Sci. Adv.* **4**, eaas9820 (2018).
9. Li, R. et al. Accelerated aging of lithium-ion batteries: bridging battery aging analysis and operational lifetime prediction. *Sci. Bull.* **68**, 3055–3079 (2023).
10. De Sutter, L. et al. Comprehensive aging analysis of volumetric constrained lithium-ion pouch cells with high concentration silicon-alloy anodes. *Energies* **11**, 2948 (2018).
11. Chu, Z. et al. Optimal charge current of Lithium Ion battery. *Energy Procedia* **142**, 1867–1873 (2017).
12. Mikheenkova, A. et al. Ageing of high energy density automotive li-ion batteries: the effect of temperature and state-of-charge. *J. Electrochem. Soc.* **170**, 080503 (2023).
13. Waldmann, T., Wilka, M., Kasper, M., Fleischhammer, M. & Wohlfahrt-Mehrens, M. Temperature dependent ageing mechanisms in lithium-ion batteries – a post-mortem study. *J. Power Sources* **262**, 129–135 (2014).
14. Raj, T., Wang, A. A., Monroe, C. W. & Howey, D. A. Investigation of path-dependent535 degradation in Lithium-Ion batteries**. *Batter. Supercaps* **3**, 1377–1385 (2020).
15. Edge, J. S. et al. Lithium ion battery degradation: what you need to know. *Phys. Chem. Chem. Phys.* **23**, 8200–8221 (2021).
16. Kuntz, P., Lonardoni, L., Genies, S., Raccurt, O. & Azaïs, P. Evolution of safety behavior of high-power and high-energy commercial Li-Ion cells after electric vehicle aging. *Batteries* **9**, 427 (2023).
17. Zeng, X. et al. Kinetic study of parasitic reactions in lithium-ion batteries: a case study on LiNi0.6Mn0.2Co0.2O2. *ACS Appl. Mater. Interfaces* **8**, 3446–3451 (2016).
18. Friesen, A. et al. Impact of cycling at low temperatures on the safety behavior of 18650-type lithium ion cells: Combined study of mechanical and thermal abuse testing accompanied by post-mortem analysis. *J. Power Sources* **334**, 1–11 (2016).
19. Shahid, S. & Agelin-Chaab, M. A review of thermal runaway prevention and mitigation strategies for lithium-ion batteries. *Energy Convers. Manag. X* **16**, 100310 (2022).
20. Mikheenkova, A. et al. Resolving high potential structural deterioration in Ni-rich layered cathode materials for lithium-ion batteries operando. *J. Energy Storage* **57**, 106211 (2023).
21. Lin, X., Khosravinia, K., Hu, X., Li, J. & Lu, W. Lithium plating mechanism, detection, and mitigation in lithium-ion batteries. *Prog. Energy Combust. Sci.* **87**, 100953 (2021).
22. Waldmann, T., Hogg, B.-I. & Wohlfahrt-Mehrens, M. Li plating as unwanted side reaction in commercial Li-ion cells – A review. *J. Power Sources* **384**, 107–124 (2018).
23. Wang, S., Rafiz, K., Liu, J., Jin, Y. & Lin, J. Y. Effects of lithium dendrites on thermal runaway and gassing of LiFePO 4 batteries. *Sustain. Energy Fuels* **4**, 2342–2351 (2020).
24. Lu, X., Tarascon, J.-M. & Huang, J. Perspective on commercializing smart sensing for batteries. *eTransportation* **14**, 100207 (2022).

25. Wei, Z. et al. Future smart battery and management: advanced sensing from external to embedded multi-dimensional measurement. *J. Power Sources* **489**, 229462 (2021).
26. Yi, Z., Chen, Z., Yin, K., Wang, L. & Wang, K. Sensing as the key to the safety and sustainability of new energy storage devices. *Prot. Control Mod. Power Syst.* **8**, 27 (2023).
27. Wickersheim, K. A. & Sun, M. H. Fiberoptic thermometry and its applications. *J. Microw. Power Electromagn. Energy* **22**, 85–94 (1987).
28. Villemin, E. et al. Thermo-luminescent optical fibre sensor for Li-ion cell internal temperature monitoring. *J. Power Sources* **593**, 233981 (2024).
29. Yu, Y. et al. Real-time monitoring of internal structural deformation and thermal events in lithium-ion cell via embedded distributed optical fibre. *J. Power Sources* **521**, 230957 (2022).
30. Mikolajek, M. et al. Temperature measurement using optical fiber methods: overview and evaluation. *J. Sens.* **2020**, e8831332 (2020).
31. Raijmakers, L. H. J., Danilov, D. L., Eichel, R.-A. & Notten, P. H. L. A review on various temperature-indication methods for Li-ion batteries. *Appl. Energy* **240**, 918–945 (2019).
32. Huang, J. et al. Operando decoding of chemical and thermal events in commercial Na(Li)-ion cells via optical sensors. *Nat. Energy* **5**, 674–683 (2020).
33. Mei, W. et al. Operando monitoring of thermal runaway in commercial lithium-ion cells via advanced lab-on-fiber technologies. *Nat. Commun.* **14**, 5251 (2023).
34. Albero Blanquer, L. et al. Optical sensors for operando stress monitoring in lithium-based batteries containing solid-state or liquid electrolytes. *Nat. Commun.* **13**, 1153 (2022).
35. Schmitt, J. et al. Measurement of gas pressure inside large-format prismatic lithium-ion cells during operation and cycle aging. *J. Power Sources* **478**, 228661 (2020).
36. Gulsoy, B., Vincent, T. A., Briggs, C. & Sansom, J. E. H. In-situ measurement of internal gas pressure within cylindrical lithium-ion cells. *J. Power Sources* **570**, 233064 (2023).
37. Yang, G., Leitão, C., Li, Y., Pinto, J. & Jiang, X. Real-time temperature measurement with fiber Bragg sensors in lithium batteries for safety usage. *Measurement* **46**, 3166–3172 (2013).
38. Tan, K. et al. Operando monitoring of internal gas pressure in commercial lithium-ion batteries via a MEMS-assisted fiber-optic interferometer. *J. Power Sources* **580**, 233471 (2023).
39. Hedman, J., Mogensen, R., Younesi, R. & Björefors, F. Fiber optical detection of lithium plating at graphite anodes. *Adv. Mater. Interfaces* **10**, 2201665 (2023).
40. Huang, J. et al. Unravelling thermal and enthalpy evolutions of commercial sodium-ion cells upon cycling ageing via fiber optic sensors. *J. Electrochem. Soc.* **170**, 090510 (2023).
41. Narayan, R., Laberty-Robert, C., Pelta, J., Tarascon, J.-M. & Dominko, R. Self-healing: an emerging technology for next-generation smart batteries. *Adv. Energy Mater.* **12**, 2102652 (2022).
42. Mezzomo, L. et al. Exploiting self-healing in lithium batteries: strategies for next-generation energy storage devices. *Adv. Energy Mater.* **10**, 2002815 (2020).
43. Huang, J., Boles, S. T. & Tarascon, J.-M. Sensing as the key to battery lifetime and sustainability. *Nat. Sustain.* **5**, 194–204 (2022).
44. Meng, Q., Huang, Y., Li, L., Wu, F. & Chen, R. Smart batteries for powering the future. *Joule* **8**, 344–373 (2024).
45. Han, X. et al. Operando monitoring of dendrite formation in lithium metal batteries via ultrasensitive tilted fiber Bragg grating sensors. *Light Sci. Appl.* **13**, 24 (2024).
46. Li, H. et al. Optical fiber sensor based on upconversion nanoparticles for internal temperature monitoring of Li-ion batteries. *J. Mater. Chem. C.* **9**, 14757–14765 (2021).
47. Wang, Y., Zhang, Q., Yang, C. & Xia, Z. Ratiometric fluorescence optical fiber enabling operando temperature monitoring in pouch-type battery. *Adv. Mater.* **36**, 2401057 (2024).
48. Li, Y. et al. Errors in the reference electrode measurements in real lithium-ion batteries. *J. Power Sources* **481**, 228933 (2021).
49. Rutz, D., Brauchle, F., Stehle, P., Bauer, I. & Jacob, T. An experimental method to determine the measurement error of reference electrodes within lithium-ion batteries. *ChemElectroChem* **10**, e202300216 (2023).
50. Wahl, M. S. et al. The importance of optical fibres for internal temperature sensing in lithium-ion batteries during operation. *Energies* **14**, 3617 (2021).
51. Yao, K. P. C., Okasinski, J. S., Kalaga, K., Shkrob, I. A. & Abraham, D. P. Quantifying lithium concentration gradients in the graphite electrode of Li-ion cells using operando energy dispersive X-ray diffraction. *Energy Environ. Sci.* **12**, 656–665 (2019).
52. Tardif, S. et al. Combining operando X-ray experiments and modelling to understand the heterogeneous lithiation of graphite electrodes. *J. Mater. Chem. A* **9**, 4281–4290 (2021).
53. Kim, M.-H. et al. Mitigating electrode-level heterogeneity using phosphorus nanolayers on graphite for fast-charging batteries. *ACS Energy Lett.* **8**, 3962–3970 (2023).
54. Kim, J. et al. Unveiling the role of electrode-level heterogeneity alleviated in a silicon graphite electrode under operando microscopy. *Energy Storage Mater.* **57**, 269–276 (2023).
55. Dahn, J. R. Phase diagram of Li x C 6. *Phys. Rev. B* **44**, 9170–9177 (1991).
56. Didier, C., Pang, W. K., Guo, Z., Schmid, S. & Peterson, V. K. Phase evolution and intermittent disorder in electrochemically lithiated graphite determined using in operando neutron diffraction. *Chem. Mater.* **32**, 2518–2531 (2020).
57. Taminato, S. et al. Real-time observations of lithium battery reactions—operando neutron diffraction analysis during practical operation. *Sci. Rep.* **6**, 28843 (2016).
58. Schmitt, C., Kube, A., Wagner, N. & Friedrich, K. A. Understanding the influence of temperature on phase evolution during lithium-graphite (De-)intercalation processes: an operando X-ray diffraction study. *ChemElectroChem* **9**, e202101342 (2022).
59. Heenan, T. M. M. et al. Mapping internal temperatures during high-rate battery applications. *Nature* **617**, 507–512 (2023).
60. Goutam, S. et al. Three-dimensional electro-thermal model of li-ion pouch cell: analysis and comparison of cell design factors and model assumptions. *Appl. Therm. Eng.* **126**, 796–808 (2017).
61. Lin, J., Chu, H. N., Howey, D. A. & Monroe, C. W. Multiscale coupling of surface temperature with solid diffusion in large lithium-ion pouch cells. *Commun. Eng.* **1**, 1–10 (2022).
62. Ghashghaie, S. et al. Towards long-term monitoring of commercial lithium-ion batteries enabled by externally affixed fiber sensors and strain-based prognostic strategies. *J. Electrochem. Soc.* **171**, 040515 (2024).
63. Berhaut, C. L. et al. Charge dynamics induced by lithiation heterogeneity in silicon-graphite composite anodes. *Adv. Energy Mater.* **13**, 2301874 (2023).
64. Schweidler, S. et al. Volume changes of graphite anodes revisited: a combined operando x-ray diffraction and in situ pressure analysis study. *J. Phys. Chem. C.* **122**, 8829–8835 (2018).
65. Peng, J. et al. State estimation of lithium-ion batteries based on strain parameter monitored by fiber Bragg grating sensors. *J. Energy Storage* **52**, 104950 (2022).
66. Guo, J. et al. Microfiber sensor integrated inside solid-state lithium-metal batteries for reducing invasiveness. *J. Power Sources* **599**, 234231 (2024).
67. Wang, X. et al. Non-damaged lithium-ion batteries integrated functional electrode for operando temperature sensing. *Energy Storage Mater.* **65**, 103160 (2024).

68. Genies, S., et al. Multi-scale multi-techniques investigations of Li-ion batteries: towards a European battery hub [dataset]. European synchrotron radiation facility. https://doi.org/10.15151/ESRF-ES-675577547 (2025).
69. Flores, E. et al. PRISMA: A robust and intuitive tool for high-throughput processing of chemical spectra. *Chem. Methods* **10**, 202100094 (2022).

Acknowledgements

Beamtime at the ESRF was granted within the Battery Pilot Hub MA4929 "Multi-scale Multi-techniques investigations of Li-ion batteries: towards a European Battery Hub" coordinated by S.L. The work was carried out in the frame of EU H2020 Research and Innovation Program projects BIG-MAP and INSTABAT, under grant agreements No. 957189 and No. 955930, respectively funding S.L., Q.J., S.T. and O.R, S.G., R.F., E.V., C.S. Both are carried out in the framework of the BATTERY2030+ large-scale initiative under grant agreement No. 957213 (S.L.). Pierre Balfet is thanked for preparing the equipped cells, and Olivier Poncelet and Sonia Sousa-Nobre for their help in manufacturing the optical fiber sensor for internal temperature measurements. Maxime Servajon is thanked for data visualization, and the first analysis was performed using his Python code.

Author contributions

S.L. and O.R. conceived the experiment. S.G. and E.V. built and equipped the cells. S.L., S.T., O.R., C.V. S.G., R.F., and C.S. performed the X-ray experiments, with O.R., R.F., C.S., S.G., and E.V. operating the sensor's detection and further analyzing the corresponding data from optical fiber and reference electrode. The beamline was aligned and set by N.B., who also helped with data processing. A.O. and S.L. analyzed the results from the XRD experiment together with O.R., S.T., C.V., Q.J., and Q.B. A.O. and S.L. wrote the manuscript with O.R., S.G., and R.F., with help from S.T., C.V., Q.B., and P.C. All authors contributed to revising the manuscript. The work of A.O. was supervised by R.P. and S.L.

Competing interests

The authors declare no competing interests.

Additional information

Supplementary information The online version contains supplementary material available at https://doi.org/10.1038/s41467-024-54656-6.

Correspondence and requests for materials should be addressed to Olivier Raccurt or Sandrine Lyonnard.

Peer review information *Nature Communications* thanks Svetlana Menkin, and the other, anonymous, reviewer for their contribution to the peer review of this work. A peer review file is available.